

2013

Flow induced vibrations of microcantilevers

<https://hdl.handle.net/2144/12119>

"Downloaded from OpenBU. Boston University's institutional repository."

BOSTON UNIVERSITY
COLLEGE OF ENGINEERING

Thesis

**FLOW INDUCED VIBRATIONS OF
MICROCANTILEVERS**

by

SETH HODSON

B.A., Bard College, 2008

Submitted in partial fulfillment of the
requirements for the degree of
Master of Science

2013

© Copyright by
SETH HODSON
2013

Approved by

First Reader

Kamil Ekinici, PhD
Associate Professor of Mechanical Engineering

Second Reader

Victor Yakhot, PhD
Professor of Mechanical Engineering

Third Reader

Taejoon Kouh, PhD
Visiting Professor of Mechanical Engineering

Acknowledgments

I would like to thank my advisor, Professor Kamil Ekinci, for his guidance in this project. I also would like to express my gratitude to Professors Victor Yakhot and Taejoon Kouh for acting as members of my thesis defense committee.

I certainly could not have accomplished anything here without the advice, assistance, and experience of my colleagues from the Nanometer Scale Engineering Lab, Charles Lissandrello and Ozgur Ozsun. Their help with everything from optics and fluid mechanics to the ins and outs of the ME department and how to make a purchase order has been invaluable.

I would also like to thank the kind and friendly students who work in the Singh Imagineering Laboratory, or Tinker Lab. Without their help in showing me how to use an NC mill for the creation of the flow chamber described herein, none of this could have happened.

Finally, I would like to thank Jessica Sirkin for keeping me sane during all of this, and being patient with me when I spent late nights at the lab.

FLOW INDUCED VIBRATIONS OF MICROCANTILEVERS

SETH HODSON

ABSTRACT

This thesis is focused on the study of flow-induced vibrations of microcantilevers. A flow chamber for testing microcantilevers under different flow rates is designed and constructed. Several cantilevers of different linear dimensions and resonant frequencies are subsequently exposed to turbulent air flow. The resulting vibrations are measured using an optical lever technique. The time traces of the vibrations are recorded as a function of flow rate. This vibration data are subsequently analyzed in frequency and time domains. It is found that the vibrations begin at Reynolds numbers (in cantilever dimensions) substantially lower than those expected for classical vortex-induced vibrations. The flow induced vibration frequencies depend weakly on the flow rates; the amplitudes increase strongly with increasing flow rates. Given that the flow in the flow chamber is turbulent, it is proposed that the vibrations result from an interaction of the resonant body with the turbulent flow. Further experiments are proposed to confirm or refute this hypothesis of turbulence-driven vibrations of microcantilevers.

Contents

1	Introduction	1
2	Background	3
2.1	Vibrations of Cantilevered Beams	3
2.2	Self-Sustaining Oscillations	4
2.3	Vortex Induced Vibration	5
2.4	Strouhal Numbers for Rectangular Bodies	8
2.5	Microcantilevers in Flow	9
3	Experimental Setup	11
3.1	Optical Beam Deflection Method	11
3.2	Spot Size Measurement	13
3.3	Flow Chamber	13
3.4	Flow Meter	16
3.5	Flow System Setup	16
3.6	Cantilevers	17
3.7	Inference of Cantilever Dimensions from Resonance Frequency	17
3.8	Forced Vibration Setup	19
3.9	Network Analyzer Measurements	20
3.10	Mode Shape Measurements	21
3.11	Mounting Angle Measurement	24
4	Experimental Results	25
4.1	Data in Time and Frequency Domains	25

4.2	Amplitude and Frequency Plots	28
5	Discussion of Results	35
5.1	Onset of Vibration	35
5.2	Lift and Dynamic Pressures	35
5.3	Comparison to Van der Pol Oscillator	37
5.4	Turbulence Force	38
6	Conclusion	42
	References	44
	Curriculum Vitae	45

List of Tables

3.1	Cantilever properties: Length L , width w , thickness t , fundamental frequency f , and spring constant k .	
	*Trapezoidal cross section.	17
3.2	Cantilever mounting angles	24
4.1	Projection Widths	33

List of Figures

3-1	Optical beam deflection setup.	12
3-2	Spot size measurement.	13
3-3	Flow chamber base	14
3-4	Flow channel detail.	14
3-5	Flow chamber assembly, exploded view	15
3-6	Block diagram of flow system setup.	16
3-7	Block diagram of network analyzer setup for forced vibration testing.	19
3-8	Lorentz fit of the frequency response of the cantilever	20
3-9	Lorentz fit of the second peak in the cantilever's frequency response.	21
3-10	First mode shape.	23
3-11	Second mode shape.	23
4-1	Time and frequency domain data for cantilever 1.	26
4-2	Time and frequency domain data for cantilever 4	27
4-3	Time and frequency domain data for cantilever 6	29
4-4	Time and frequency domain data for cantilever 7	30
4-5	Scaled amplitude as a function of flow velocity.	31
4-6	Scaled amplitude as a function of dimensionless flow velocity.	31
4-7	Frequency and Reynolds number data for cantilevers 1, 6, and 7.	32
4-8	Frequency and Reynolds number in reference to stream projection width.	33
4-9	Amplitude and Reynolds number data in reference to stream projection width.	34

5.1	Relative amplitude as a function of lift pressure for cantilevers 1, 6, and 7.	36
5.2	Relative amplitude and dynamic pressure for cantilevers 1, 6, and 7. .	37
5.3	Dimensionless amplitude and dynamic pressure.	38
5.4	Turbulence in the macroscopic flow induces a varying force on the face of the cantilever.	39
5.5	Thermal noise oscillations for cantilever 1. The quality factor of the Lorentz fit function is 365.	39
5.6	Scaled amplitude as a function of the Reynolds number in reference to channel dimensions.	41

Chapter 1

Introduction

The microcantilever has excited a great deal of interest in the research community in recent years. In addition to its applications in atomic force microscopy, for which the fabrication of microcantilevers first began, its low active mass and small size make it a very sensitive measurement device, and it has shown great promise in fluid studies and lab-on-a-chip applications.

The interaction between a flowing fluid and the cantilever structure is of particular importance to these applications. For slowly flowing fluids, the cantilever deflects statically, but beyond some critical flow velocity, large vibrations begin. While this static deflection of a cantilever at low Reynolds numbers has been studied (Jana et al., 2007), the mechanism by which instabilities develop to induce the vibrations observed at higher Reynolds numbers is largely unexplored in the literature.

The behavior of a cantilevered beam undergoing oscillation is well understood in the field of vibrational mechanics. The cantilever has a set of natural frequencies depending on its physical characteristics. When a periodic force is exerted on the cantilever, it responds with large amplitude vibrations when the frequency of the forcing is at or near these natural frequencies. The application of this to microcantilevers is laid out by Paolino et al. (Paolino et al., 2009). This study focused on the spatial modes of the microcantilever, and measured them using an optical lever system similar to that used in the present study, finding a good agreement with theoretical spatial modes (Ginsberg, 2001).

It is possible that the interaction between the cantilever and a flowing fluid can

be characterized as a vortex-induced vibration. This phenomenon has been studied by numerous authors, notably the early seminal work by Feng, as well as a number of recent experiments and numerical analyses reviewed in bulk by Bearman and Williamson (Feng, 1969; Bearman, 1984; Williamson and Govardhan, 2004). These, however, have focused largely on macroscopic bodies with comparatively low resonance frequencies. Vibrational systems with the frequency range and length scale of the microcantilever have not been studied thoroughly in the context of vortex induced vibration.

It is the goal of this thesis to examine the vibration of the microcantilever in flowing fluid to determine the underlying physics of the system.

Chapter 2

Background

2.1 Vibrations of Cantilevered Beams

A simple cantilevered beam, of uniform cross section and material properties, has a series of natural modes of vibration. These are analogous to the standing waves found on vibrating strings: the result of reflection at each end appropriate to the relevant boundary condition. However, the boundary conditions of the cantilever require that both the displacement and its first spatial derivative be zero at the base of the cantilever, while the other end of the cantilever is free. This changes the ratio of fundamental frequencies such that they are not a harmonic series, unlike the standing wave.

The resonance frequencies of a cantilever of width w , thickness t and length L are

$$f_n = \frac{\alpha_n^2}{2\pi} \sqrt{\frac{EI}{\rho wt L^4}} \quad (2.1)$$

where α_n^2 is the modal coefficient for the n th mode, E is the Young's modulus, and I is the second moment of inertia. The modal coefficients are given by

$$1 + \cos \alpha_n \cosh \alpha_n = 0 \quad (2.2)$$

The spatial modes are of interest as well. These are given by

$$\psi_n \left(\frac{x}{L} \right) = \left[\cos \left(\alpha_n \frac{x}{L} \right) - \cosh \left(\alpha_n \frac{x}{L} \right) \right] - \frac{\cos \alpha_n + \cosh \alpha_n}{\sin \alpha_n + \sinh \alpha_n} \left[\sin \left(\alpha_n \frac{x}{L} \right) - \sinh \left(\alpha_n \frac{x}{L} \right) \right] \quad (2.3)$$

Comparison of physical measurements of a cantilever's deflection to this formula can be used to assess the capability of the measuring system.

Each resonance frequency denotes a peak in the frequency response of the vibrating system. The behavior of the system near these peaks can be modeled as a damped harmonic oscillator. This system is described by the differential equation

$$m\ddot{x} + c\dot{x} + kx = F(x) \quad (2.4)$$

where x represents the relevant modal coordinate, in this case the cantilever deflection, and $F(t)$ is an external forcing function of time; m , c , and k represent the lumped mass, energy dissipation, and force constants. This ideal system has a resonance frequency defined as

$$f_{DHO} = \frac{1}{2\pi} \sqrt{\frac{k}{m}} \quad (2.5)$$

When modeling a cantilever as a damped harmonic oscillator, the frequency f_{DHO} can be any of the resonance frequencies f_n . The values of the lumped parameters m and k depend on the modal coefficient.

2.2 Self-Sustaining Oscillations

A self-sustaining oscillator can be created if a portion of the vibrational signal is amplified and fed back to the system as a driving force. If the phase and amplitude meet the necessary criteria, positive feedback is achieved and the resonator becomes an oscillator. An example of this is the Van der Pol oscillator, whose equation of motion with zero forcing is

$$\ddot{x} - (\lambda - x^2)\dot{x} + (2\pi f_n)^2 x = 0 \quad (2.6)$$

The effect of the damping term in this equation of motion is that the amplitude of the vibrations will be increased if small, but reduced if large. The Van der Pol oscil-

lator would be identifiable by three properties: its self-sustained nature, its limited amplitude, and, most significantly, its entrainment of external driving frequency to its own natural frequency f_n .

In a fluid-structure interaction, the Van der Pol oscillator is a useful model for the entrainment of fluid. In an ordinary damped harmonic oscillator described by equation 2.4, the damping coefficient c represents viscous drag on the body as it moves through the still fluid. However, if the fluid is brought into motion in concert with the motion of the body, the damping will vary depending on the degree to which this occurs, which will, in turn, depend on the amplitude of the vibration. The relation between these is the physical interpretation of the parameter λ in equation 2.6.

2.3 Vortex Induced Vibration

Numerous studies have also been performed in relation to vortex-induced vibrations. A bluff body in a flowing viscous fluid is known to create vortices in its wake. The vortices are shed from the body in a Von Karman vortex street, at a frequency depending on the flow velocity and body diameter. This is described by the Strouhal number, defined as

$$St = \frac{f_v D}{U} \quad (2.7)$$

where f_v is the vortex shedding frequency, D is a characteristic length (in the case of the circular cylinder, the diameter), and U is the flow velocity. One way to interpret this number is the ratio of the characteristic length D to the distance U/f_v between shed vortices in the wake.

The Strouhal number can be expressed as a slowly varying function of the Reynolds

number. The Reynolds number is defined as

$$Re = \frac{UD\rho}{\mu} \quad (2.8)$$

and is a useful expression of the degree of turbulence in a fluid flow. It compares the effects due to fluid momentum, $U\rho$, to the effects due to viscous forces, μ/D .

The Strouhal number is considered to be a known quantity for circular cylinders (Feng, 1969; Fujarra et al., 2001). Williamson defines a universal Strouhal-Reynolds curve for circular cylinders with parallel vortex shedding (Williamson, 1988). However, for cylinders of rectangular cross section such as the microcantilevers in question, the value of the Strouhal number for various geometries and Reynolds numbers is less clearly defined. Further discussion on this topic appears below.

In addition to the Reynolds number, it is common to consider vortex shedding in terms of nondimensionalized parameters. These include the dimensionless flow velocity,

$$U^* = \frac{U}{f_n D} \quad (2.9)$$

and the dimensionless frequency,

$$f^* = \frac{f}{f_n} \quad (2.10)$$

These dimensionless quantities are useful when comparing vortex induced vibration behaviors of bodies with differing geometries and natural frequencies.

A notable result of these experimental and numerical studies is that of lock-in, wherein the vortex shedding frequency is forced into alignment with the natural frequency of the vibrating body. This is typically characterized in a graph of normalized flow velocity versus normalized vibration amplitude and frequency. The occurrence of lock-in is shown by Feng in several such plots under different damping coefficients to coincide with a large increase in amplitude (Feng, 1969). The amplitude rises during an initial branch as the flow velocity increases. The upper branch is defined as the

region when the ideal vortex shedding frequency, based on the Strouhal number for a fixed body, becomes close to the natural frequency of the resonant body. At this critical flow velocity, the amplitude reaches its maximum and lock-in occurs, with the vortex shedding frequency forced to closely match the natural vibration frequency. This level is maintained until the true vortex shedding frequency abruptly increases beyond the natural frequency. The amplitude of the vibrations decrease once more, forming a lower branch. Many studies have focused primarily on circular cylindrical bodies on springlike mounts that exhibit the behavior of one- or two-dimensional harmonic oscillators. It is these that exhibit the three-branch system.

A more directly relevant experiment was conducted by Fujarra et al (Fujarra et al., 2001). This study measured the oscillations of cantilevered cylindrical beams with internal flexible aluminum plates. The plate allows a much greater degree of flexibility in the transverse direction than the streamwise direction, making it similar to the microcantilevers used in the present experiment. It is important to note that the cantilevers' external profile was round in this experiment, which is an important factor in determining the Strouhal number. The size of the cantilevered beams is also many times that of the microcantilevers studied here: Fujarra's cantilever has a characteristic length of 10 millimeters, some two thousand times larger than the thickness of a microcantilever.

Fujarra found that the cantilevered beams, unlike elastically mounted beams, exhibit only an initial and lower branch of amplitudes, rather than the three-branch system described by Feng found for elastically mounted cylinders. Fujarra also observed lock-in occurring when the vortex shedding frequency, taken from the assumed Strouhal number for the range of Reynolds numbers in question, came close to the fundamental resonance frequency of the cantilever. As the dimensionless velocity U^* passed a value of about 7, the amplitude was reduced slightly and the frequency set-

bled at a value between the resonance frequency and the vortex shedding frequency. Additionally, the study documented high-frequency vibrations beyond the resonance frequency occurring at $U^* > 10$, and it was proposed that this was due to a synchronization effect between the cantilever's transverse and streamwise vibrational modes.

2.4 Strouhal Numbers for Rectangular Bodies

Since the vortex shedding frequency is not measured directly in the present experiment, it must be inferred from the Strouhal number. Fugarra's experiment, as well as many other publications in the literature, focuses primarily on vortex shedding from a cylindrical body of circular cross-section. Feng takes the Strouhal number for a circular cylinder to be a known quantity, and fixed for the Reynolds numbers of interest in that study. Though a D-section cylinder is also considered in Feng's study, the Strouhal number for that structure is not mentioned. Because non-circular bodies are the subject of the present experiment, the Strouhal number is not as well-known as in the case of Fugarra's study.

Strouhal numbers for cylinders of rectangular cross section are examined in a numerical simulation by Sohankar et al. (Sohankar et al., 1997). The emphasis of the study is on the effects of several parameters on the Strouhal number, including Reynolds number, aspect ratio, and angle of incidence. The Strouhal number is found to increase steadily from $Re = 50$ to $Re = 100$ for a square cylinder, leveling off around 0.15 and beginning to drop by $Re = 400$. It is also noted that the angle of incidence is an important factor in the Strouhal number, with a particularly steep slope when the angle is close to zero; that is, the difference in Strouhal number between a rectangular body with its longer face parallel to the flow and the same body only slightly off-parallel is significant. To that end, it will be necessary in this study to know the precise angle of incidence for the cantilevers with respect to the

fluid flow.

2.5 Microcantilevers in Flow

Microcantilevers have been studied in flowing viscous fluids by Jana et al. (Jana et al., 2007). This experiment focused on the deflection of cantilevers in dry nitrogen gas flow. The cantilevers were placed in line with the flow of gas through a flow chamber at varying volumetric flow rates. The flow rate was increased in steps from 20 mL/min to 160 mL/min. A numerical simulation was conducted to predict the flow velocity redirected into the face of the cantilever around its mounting chip. From this simulation, an estimate of the drag force on the cantilever could be generated. For flow rates below 150 mL/min, a linear relationship was found between the flow rate and the deflection of the cantilever tip. Beyond this flow velocity, instabilities in the fluid-structure system induced large vibrations in the cantilever. However, the analysis conducted by the authors was limited to the domain below 150 mL/min, where the flow did not induce vibrations.

The relationship between the drag coefficient C_N of the cantilever and the Reynolds number Re_N , where the subscript indicates the numbers corresponding to the velocity component normal to the face of the cantilever, was written as

$$\ln C_N = \beta + \gamma \ln Re + \delta (\ln Re)^2 \quad (2.11)$$

where values of the coefficients β , γ , and δ are to be determined through numerical simulation.

Because this study focused entirely on static deflections, its results are of limited use in studying the vibrating cantilever. Moreover, the experimental setup described below places the cantilever in a different orientation with respect to the flow direction, such that the normal component of the velocity is zero at low flow rates. At higher

flow rates, the onset of vibration can be observed.

Chapter 3

Experimental Setup

3.1 Optical Beam Deflection Method

The deflection of a cantilever can be measured using the method of optical beam deflection. In this method, a laser is incident on the reflective surface of the cantilever. As the cantilever deflects, the angle of the reflective surface changes a small amount, deflecting the beam. The deflection of the beam can be measured a variety of ways (Garcia-Valenzuela, 1997). The method of detection used here is the knife edge, wherein the beam is partially blocked from a single photodetector. The center of the Gaussian beam is located at the edge of the blocking plate when the cantilever is not deflected. The simplicity of this method is its key advantage, as only a single photodetector is needed to sense the deflection of the beam.

Two methods were used to achieve knife-edge measurement of cantilever deflection. The first is a photosensitive silicon chip with metal deposited over part of its surface. The straight edges of the metal depositions formed the knife edge. The beam was focused on this using a converging lens of focal length 125mm. This photodetector was found to be of limited use due to the capacitive effect of the silicon chip. As laser intensity increased, the voltage across the contacts of the photodetector reached a limit, causing distortion in the waveform's measurement. Additionally, the power output of the photodetector per unit incident light intensity was found to be insufficient to measure low amplitude vibrations.

The second photodetector used was a New Focus model 1621. It was utilized with the internal 10 k load resistor. Its silicon detector is circular with a diameter of 0.8

mm. To achieve the knife-edge effect with this photodetector, the beam was partially blocked at a point between the cantilever and the photodetector, as shown in figure 3-1. The blocking screen was composed of cleaved silicon to ensure a smooth, straight knife edge. The blocking screen was mounted on a ring such that it could be rotated arbitrarily. The purpose of rotating the block is twofold: first, small deviations in the angle at which the cantilever is mounted, and therefore the angle at which the beam is deflected, could be accounted for to ensure maximum sensitivity; second, it would be possible to detect beam deflection at an angle orthogonal to the orientation of the cantilever, allowing for the possibility of detecting torsional vibrations.

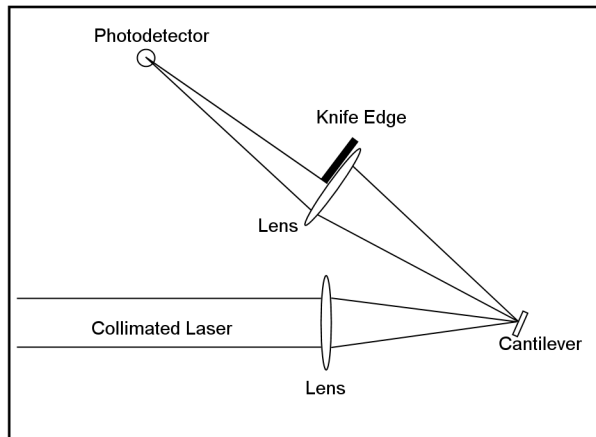


Figure 3-1: Optical beam deflection setup.

The optimal placement of the blocking screen for the second knife-edge setup was found to be near the focusing lens. Because the beam's deflection angle is greatest at this point, the finest control of the blocking screen's position relative to the beam's center is possible there. The greater diffraction compared to a blocking screen closer to the photodetector was determined to be of lesser significance, as precise placement of the blocking screen is critical for the function of the knife edge.

3.2 Spot Size Measurement

To determine the size of the laser spot at the position of the cantilever, the photodetector with metal depositions was placed at the sample location. The voltage output of the photodetector was measured as its position was advanced at intervals of five microns. This was used to determine what fraction of the beam is incident on the sensitive portion of the photodetector; the spatial derivative of that function can then be used to infer the intensity of the beam as a function of position. The spatial derivative was approximated as the difference between measurement points. The intensity of the beam was found to be a Gaussian function, as expected. Averaged over three trials, its full width at half maximum was found to be 35 microns, as shown in figure 3-2.

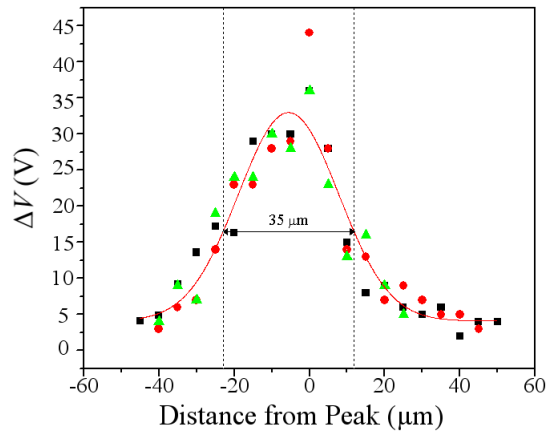


Figure 3-2: Spot size measurement.

3.3 Flow Chamber

The flow chamber, shown in figures 3-3-3-4, consists of a slab of ABS with a channel 500 microns deep and 8 mm wide cut into it. The channel connects two holes in the block spaced 30 mm apart. Surrounding this channel is a groove 600 microns wide

and 425 microns deep. The groove houses an O-ring gasket with a diameter of 30 mm and a thickness of 600 microns. The gasket seals the flow chamber to a glass slide that is held to the chamber by a cover plate. The cover plate has a slot cut into it exposing the glass over the channel, and is secured by 8 thumb screws. A microcantilever is attached to the glass slide with epoxy and positioned in the center of the channel.

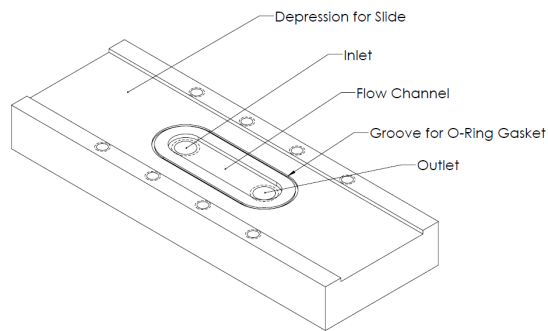


Figure 3-3: Flow chamber base

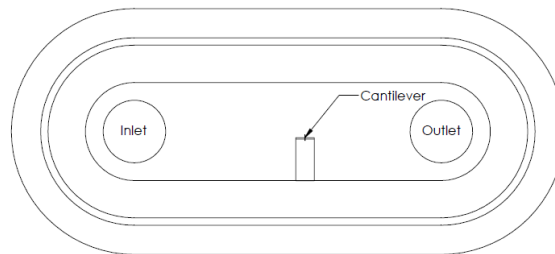


Figure 3-4: Flow channel detail.

The design of the flow chamber underwent several iterations. Initially, it had been planned to attempt to induce oscillations in the microcantilevers using water flow driven by a syringe pump. However, the flow velocities required to achieve a Reynolds number of 50 or more with respect to the dimensions of the cantilever were too large for the available equipment to achieve with a flow chamber of dimensions large enough to contain the chip on which a microcantilever is mounted. An intermediate plan with a channel whose side was cut to include a chip at its edge, the cantilever

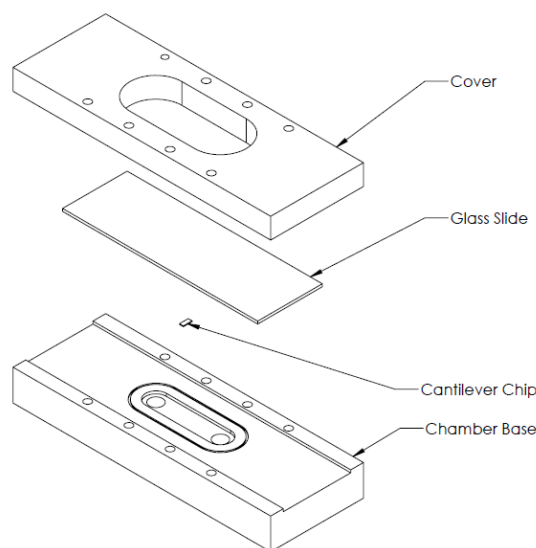


Figure 3-5: Flow chamber assembly, exploded view

protruding into the flow channel, was considered. However, fabrication and sealing difficulties prevented this design from proceeding. Additionally, the achievement of high flow rates by way of narrowing the channel was determined to cause a large pressure drop through the channel. As the syringe pump was unlikely to be capable of the mechanical power output needed to overcome such a pressure drop, the notion was abandoned. The subsequent plan was to achieve greater flow velocities using dry nitrogen gas from a compressed storage. This offered the advantage of high pressure, permitting a broad range of flow rates. The flow chamber described above was constructed with this purpose in mind. However, it was subsequently determined that the flow rates required for the experiment caused undue waste of the limited supply of nitrogen gas. The experimental setup was altered to utilize compressed air, which was available in ample supply, and the similarities in density and viscosity between nitrogen gas and air meant that no alterations to the flow chamber were required.

3.4 Flow Meter

The flow meter used is a rotameter with a maximum measured flow rate of 12,058 mL/min of air. It has a tolerance of 2% of its maximum flow rate, or 241 mL/min. A valve at the inlet of the flow meter controls the flow of air through the system.

The rotameter functions by way of varying the area through which the fluid can flow. A spherical float is pushed up by the drag force from the flow. As it rises, the area of the tube surrounding it increases, reducing the local flow velocity and, therefore, the drag force lifting the float. The float reaches an equilibrium point within a short time, and the velocity can be inferred from the height of the equilibrium point.

3.5 Flow System Setup

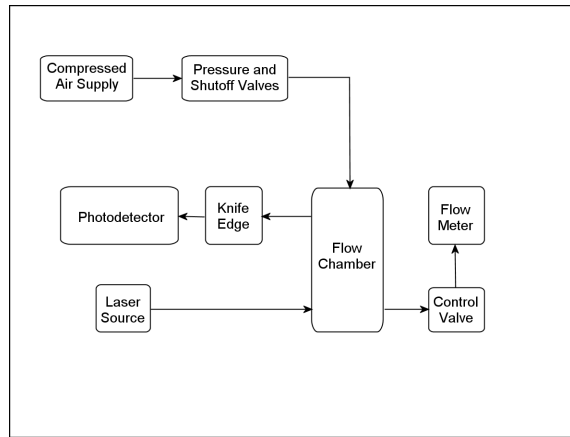


Figure 3-6: Block diagram of flow system setup.

The flow system setup is shown in figure 3-6. Compressed air at 200 kPa travels through a Teflon tube of 3/16 in. inner diameter and 10 ft. length. The input pressure is controlled by a valve at the head of the tube. A second valve is in place to quickly turn air flow on or off. The other end of the tube is connected to the inlet of the flow chamber. The flow chamber's outlet is connected by a ten-inch tube of the same type as the first length of tube to the flow meter. The flow meter's outlet

Cantilever	L (μm)	w (μm)	t (μm)	f (kHz)	k (N/m)
1	225	46	5.5	148.5	28.4
2	225	25-60*	–	125	–
3	225	50	–	175	–
4	450	38	1.5	10	0.06
5	235	25	–	225	–
6	225	40-50*	5.9	163.7	34.3
7	230	37	2.6	70.4	2.26

Table 3.1: Cantilever properties: Length L , width w , thickness t , fundamental frequency f , and spring constant k .

*Trapezoidal cross section.

releases the air into atmosphere.

3.6 Cantilevers

Seven cantilevers were tested in flow, and one was tested in forced vibration. The flow-tested cantilevers have been numbered one through seven. Their dimensions and resonance frequencies are shown in table 3.1. The thickness of the cantilevers could not be measured with available equipment; the method described below was used to derive the thickness and spring constant of each cantilever in the table.

The cantilever used in the forced vibration test with a piezoelectric actuator had a length of 450 microns and a width of 50 microns. Its resonance frequency was measured, using a piezoelectric oscillator and a network analyzer, as 12.23 kHz. The process is described below.

3.7 Inference of Cantilever Dimensions from Resonance Frequency

The cantilevers used in the present experiment were of unknown dimensions. While measurement of the length and width was achieved using a microscope, the difficulty inherent in securing the chip in a sideways orientation made measurement of the thickness impossible through the same method. However, the thickness is a critical factor in the flow characteristics as well as the resonance frequencies. It was therefore

necessary to find an alternate way to determine the thickness of the cantilevers. The resonance frequencies of a cantilevered beam are given by equation 2.1 above. For a beam of rectangular cross section bending across the t dimension, the second moment of inertia I is

$$I = \frac{wt^3}{12} \quad (3.1)$$

Because of the anisotropic crystalline structure of silicon, the Young's modulus E is not easily defined. A study by Hopcroft et al. on the anisotropic properties of monocrystalline silicon provides a detailed analysis of the correct values to use for MEMS systems like the cantilevers in question (Hopcroft et al., 2010). The selection of the most accurate value of the Young's modulus depends on the orientation of the structure with respect to the silicon crystal. It was determined based on industry standards most commonly used in scientific research that, for most cases of fabricated MEMS devices, the X and Y axes of the device—in the case of a microcantilever, the dimensions along and across the cantilever, respectively—will be oriented with the $\langle 110 \rangle$ silicon crystal directions. The appropriate value of the Young's modulus for this orientation is 169 GPa. Equation 2.1 above can be combined with equation 3.1 to solve for t if the other dimensions and the first resonance frequency f are known:

$$t = \frac{4\pi L^2 f}{\beta^2} \sqrt{\frac{3\rho}{E}} \quad (3.2)$$

This method of deducing the thickness was tested on a cantilever of known dimensions and found to be accurate to within the manufacturer's dimensional tolerances.

With the dimensions L , w , and t known, the spring constant k for the cantilever can be calculated. It is given by

$$k = \frac{Ewt^3}{4L^3} \quad (3.3)$$

3.8 Forced Vibration Setup

The setup for forced vibration is shown in figure 3-7. A collimated laser is incident on a converging lens of focal length 125 mm. This focuses the beam on the cantilever to a spot size (full width at half maximum) of 35 microns. The cantilever is mounted on a piezoelectric actuator. The piezoelectric actuator is controlled by a function generator. The diverging reflected light from the cantilever is refocused by another lens of focal length 125mm, placed at a distance greater than 125mm from the cantilever. The refocused beam is incident on the photodetector. The photodetector is a silicon chip with a metal coating over part of its surface. The beam reflected from the undisturbed cantilever is aligned such that its center is incident on the edge of the metal coating of the photodetector. When the cantilever vibrates, the beam is deflected by a small degree. The knife edge on the photodetector blocks a portion of the beam depending on the angle of deflection, such that the power output of the photodetector is controlled by the deflection of the cantilever. The photodetector acts

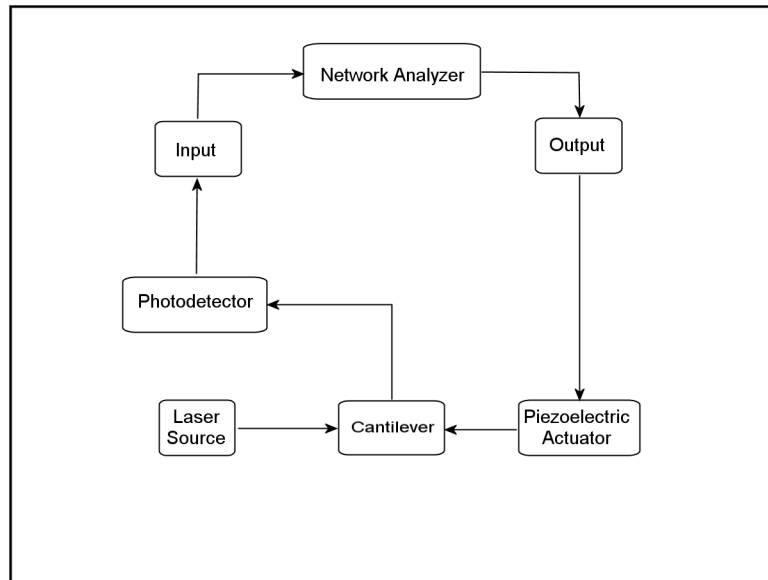


Figure 3-7: Block diagram of network analyzer setup for forced vibration testing.

as a current source, which is converted to a voltage with a 1.0 MOhm resistor. An oscilloscope is connected in parallel to the resistor and measures the voltage output from the photodetector. From this, the angle of deflection can be inferred as described above.

3.9 Network Analyzer Measurements

The piezoelectric oscillator setup described above was connected to a network analyzer to measure the frequency response over a wide range. A cantilever 450 microns in length was tested in a 60-second sweep over the range from 5 to 150 kHz. Peaks were observed near 12 kHz and 77 kHz. These peaks were then sampled at a finer resolution to more precisely identify the resonance frequency and quality factor.

The first peak was sampled over a range from 10 kHz to 14 kHz in a 10 second sweep. As shown in figure 3-8, the resonance frequency was found to be 12.23 kHz, with a quality factor Q of 54. The second peak was sampled over a range from 74

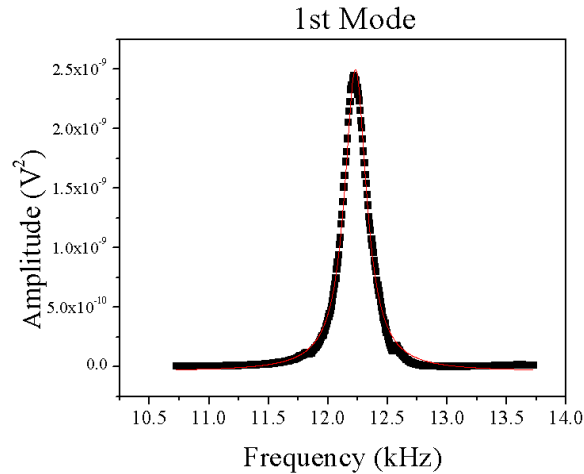


Figure 3-8: Lorentz fit of the frequency response of the cantilever

kHz to 81 kHz in a 10 second sweep. As shown in figure 3-9, the resonance was found at 77.3 kHz, with a quality factor of 152. The ratio between first and second resonance modes was therefore found to be 6.32, which is in good agreement with a

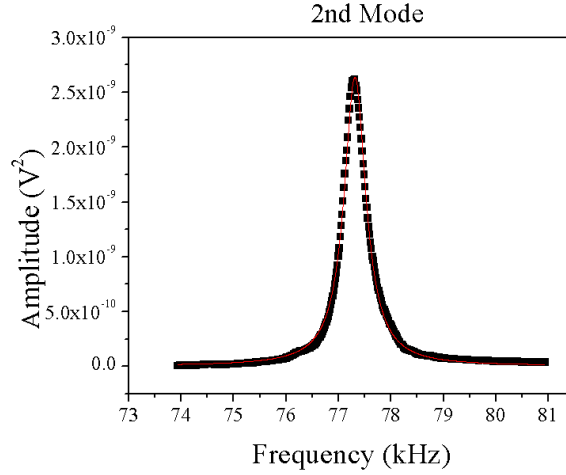


Figure 3-9: Lorentz fit of the second peak in the cantilever's frequency response.

ratio of $2/1 = 6.27$ as the ideal (Paolino et al., 2009; Ginsberg, 2001). Additionally, phase transitions were observed at both peaks. Taken together, these confirm the resonance frequencies measured and identify 12.23 kHz as the first resonant mode of the cantilever measured.

More importantly, this measurement confirmed that the optical measurement device has the needed sensitivity to capture the vibrations of a microcantilever.

3.10 Mode Shape Measurements

To further confirm the efficacy of the measurement system and the resonance modes of the cantilever in question, mode shape measurements were performed on a the above 450-micron cantilever with 12.23 kHz fundamental frequency.

The laser spot was placed initially at the base of the cantilever while the piezoelectric actuator drove its vibrations at one of the two measured modes. A measurement of the amplitude of the beam deflection was taken and the spot was advanced along the length of the cantilever by a distance of 25 microns. These measurements were repeated for the full length of the cantilever.

For the first mode, a series of 6,000 data points with a time interval of 60 nanoseconds was taken for each point along the cantilever's length. The data was then used to calculate the root-mean-square amplitude of the beam deflection.

Because the beam deflection is a function of the angle of the cantilever's deflection rather than its deflected position, the small-angle approximation

$$\theta \approx \tan \theta = \frac{dy}{dx} \quad (3.4)$$

was applied to the data points, where θ is the angle of the cantilever, y is its deflection, and x is a dimension along its length. This approximation permits the calculation of the absolute deflection as a function of x by the differential equation

$$C_1 \frac{dy}{dx} = f(x) \quad (3.5)$$

whose solution is

$$y = \frac{1}{C_1} \int f(x) dx \quad (3.6)$$

wherein C_1 is a scaling factor between the angular displacement of the beam and the voltage output of the photodetector. This solution can be approximated by the trapezoidal method:

$$y(x) \approx \frac{1}{C_1} \sum_{n=0}^{N(x)} \Delta x \frac{a_n + a_{n+1}}{2} \quad (3.7)$$

wherein Δx is the space between measured points, in this case 25 microns, a_n is the data point corresponding to the iterator n , and $N(x)$ is one plus the number of data points between $x = 0$ and the present location.

Using these methods, we can find the mode shapes for each resonant frequency of the cantilever. The first two are shown in figures 3-10 and 3-11.

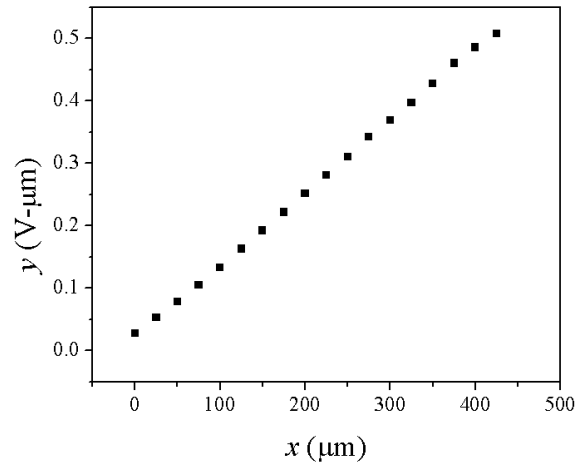


Figure 3-10: First mode shape.

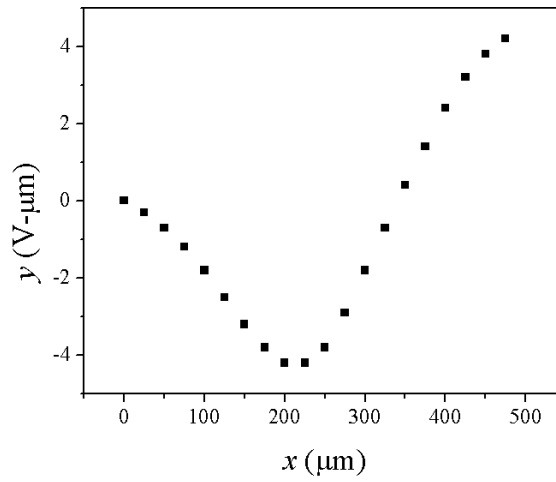


Figure 3-11: Second mode shape.

3.11 Mounting Angle Measurement

Because the angle at which the flow strikes the cantilever is critical, a precise measurement of the angle at which each cantilever is mounted to the glass slide is needed. The cantilevers are secured to the slide with epoxy by hand, so some deviation in angle is possible. To measure this, a beam was aligned with the cantilever, as in vibration measurements. The beam reflected from the cantilever can be distinguished from the beam reflected from the face of the glass slide by its diffraction pattern; the cantilever's reflection diffracts analogously to a beam of light going through a single thin slit. The horizontal and vertical distance between these beams was measured on a screen placed a known distance from the point of reflection; the angle between the two could then be determined by the relation

$$\theta_i = \arctan \frac{d_i}{d_o} \quad (3.8)$$

where θ_i and d_i are the angle and deflection length in the relevant direction, and d_o is the distance between the cantilever and the screen on which the measurement is conducted.

The angles found for each measured cantilever are shown in Table 3.2. These are

Cantilever	Angle (degrees)
1	9.6
6	0.4
7	0.4

Table 3.2: Cantilever mounting angles

important because they indicate the incident angle of the flow to the cantilever, which is necessary to accurately assess the Strouhal number (Sohankar et al., 1997).

Chapter 4

Experimental Results

Of the seven cantilevers tested in flow, four were found to begin periodic vibration at flow velocities measurable with the available equipment. These were the cantilevers that had been labeled 1, 4, 6, and 7. Vibrations were observed for cantilevers 2, 3, and 5 as well, but at flow rates too large for the flow meter to measure. The data from these cantilevers has been omitted.

The vibrations were measured for 100 milliseconds at a sampling rate of 1.25 MHz. The flow rates were varied over the range for which vibrations were observed up to the maximum flow rate of 12,058 mL/min.

4.1 Data in Time and Frequency Domains

To perform frequency domain analysis, the time-traced beam deflections were auto-correlated and a fast Fourier transform (FFT) was applied. The square root of this function is the spectral density. This can be used to measure the frequency domain characteristics of the waveform.

The time and frequency domain data for cantilever 1 at selected flow velocities are shown in figure 4-1. Cantilever 1 was found to have a strong response from flow velocities above 37.85 m/s. The response of the cantilever is noise-dominated at all flow velocities, but above this critical flow rate, large vibrations at the resonance frequency are observed.

The FFTs and time traces for cantilever 4 are shown in figure 4-2 for selected velocities. The vibration of cantilever 4 was found to be too large for the measurement

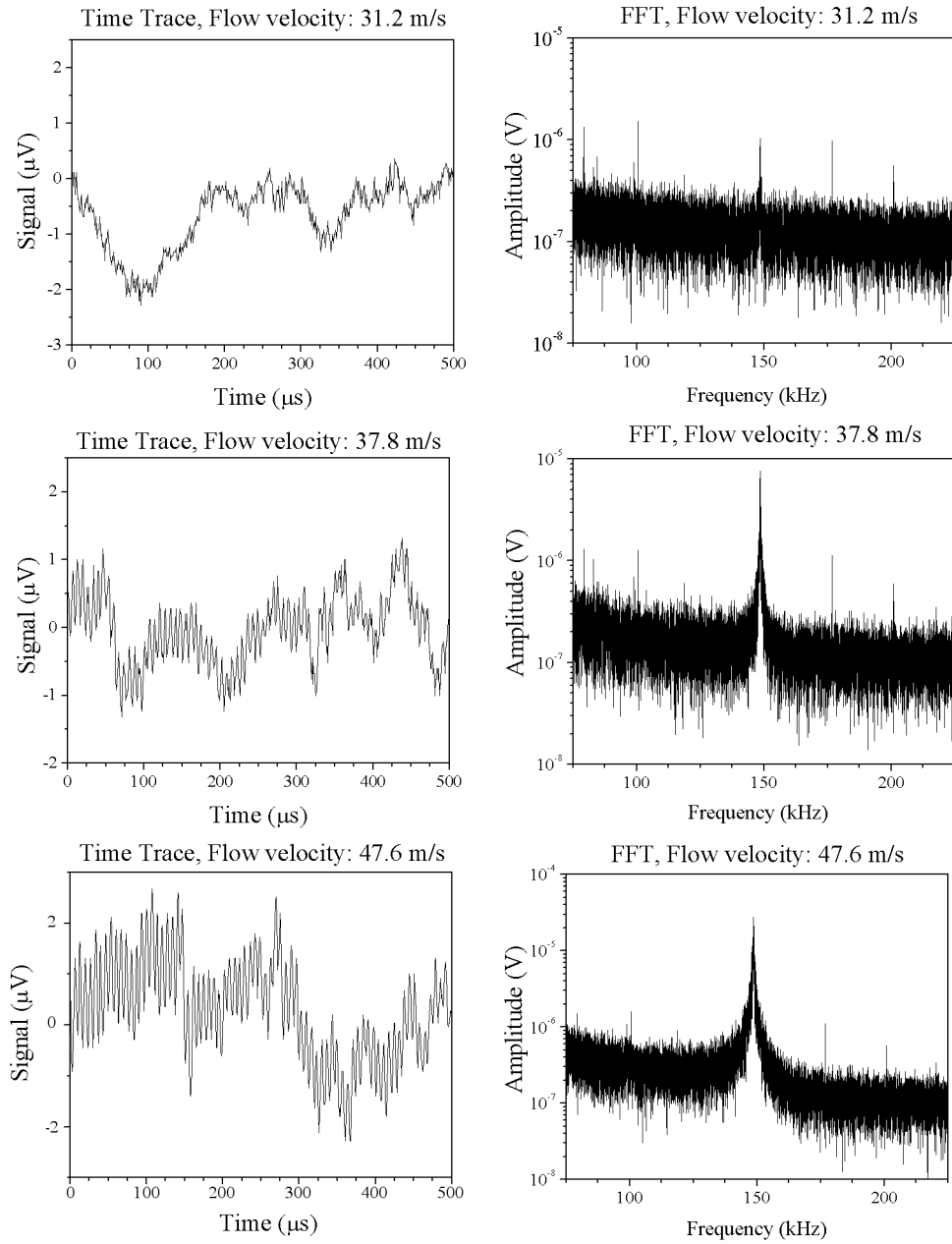


Figure 4-1: Time and frequency domain data for cantilever 1.

system. The beam was deflected off the edge of the photodetector, causing distortion in the measured waveform. As amplitude increased, the waveform reached the limit of the sensor's range, as shown in the figure. The series rising from the cantilever's 10kHz fundamental frequency at higher velocities is a result of this distortion and should not be construed as a nonlinear physical behavior. An attempt was made to reduce this factor by measuring deflection closer to the base of the cantilever and focusing the deflected beam with additional lenses of shorter focal length (20mm), resulting in an undistorted waveform up to a flow velocity of 10 m/s. After this point, distortion of the wave form was evident, and amplitude data cannot be used.

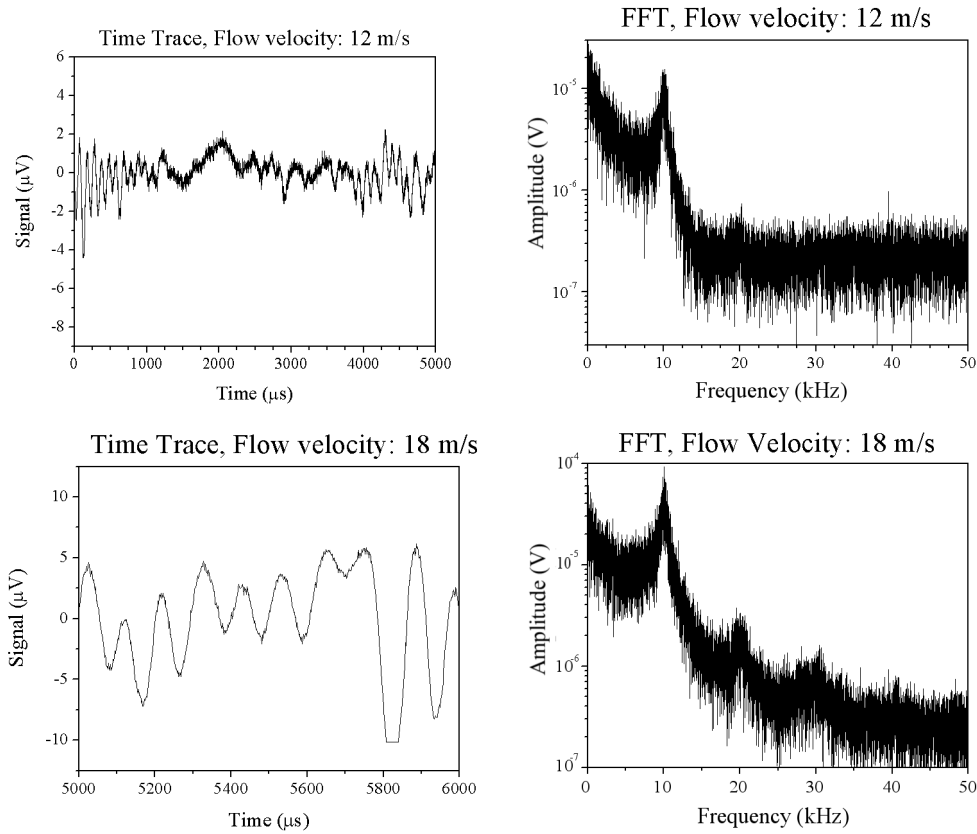


Figure 4.2: Time and frequency domain data for cantilever 4

Cantilevers 6 and 7 showed significantly smaller periodic responses than cantilevers 1 and 4. Selected time traces and FFTs for Cantilever 6 are shown in figure 4.3, and

those for cantilever 7 are shown in figure 4.4. As shown in figures 4.3 and 4.4, each of these cantilevers was primarily found to deflect randomly, with the noise signal increasing in strength as flow velocity increases. However, periodic components were observed close to the resonance frequency starting at some critical velocity for each cantilever, and increasing as flow velocity increased. Cantilevers 1 and 4, shown in figures 4.1 and 4.2, also have strong noise components, but the oscillatory behavior becomes dominant at higher velocities.

4.2 Amplitude and Frequency Plots

The amplitude of the vibration is expressed here as the dimensionless amplitude A_s , defined by

$$A_s = \frac{A}{A_{max}} \quad (4.1)$$

The amplitude as a function of the flow velocity is shown in figure 4.5. The amplitude as a function of the dimensionless velocity U^* , defined in equation 2.9, is shown in figure 4.6. While cantilevers 1 and 6 become very well collapsed, cantilever 7, which has a larger difference in dimensions and resonance frequency than the first cantilevers, is very different on this graph. The fact that the dimensionless variable of classical vortex-induced-vibration study does not collapse vibration data from cantilevers of different properties makes it somewhat less useful in this study. Another dimensionless parameter that could be useful to characterize the flow is the Reynolds number. To determine the Reynolds number for compressible flow, it is necessary to find the density based on the pressure. For the flow system in use, shown in figure 3.6 above, the greatest pressure drop is found at the flow rate control valve. The absolute pressure inside the flow chamber is therefore assumed equal to the input pressure of

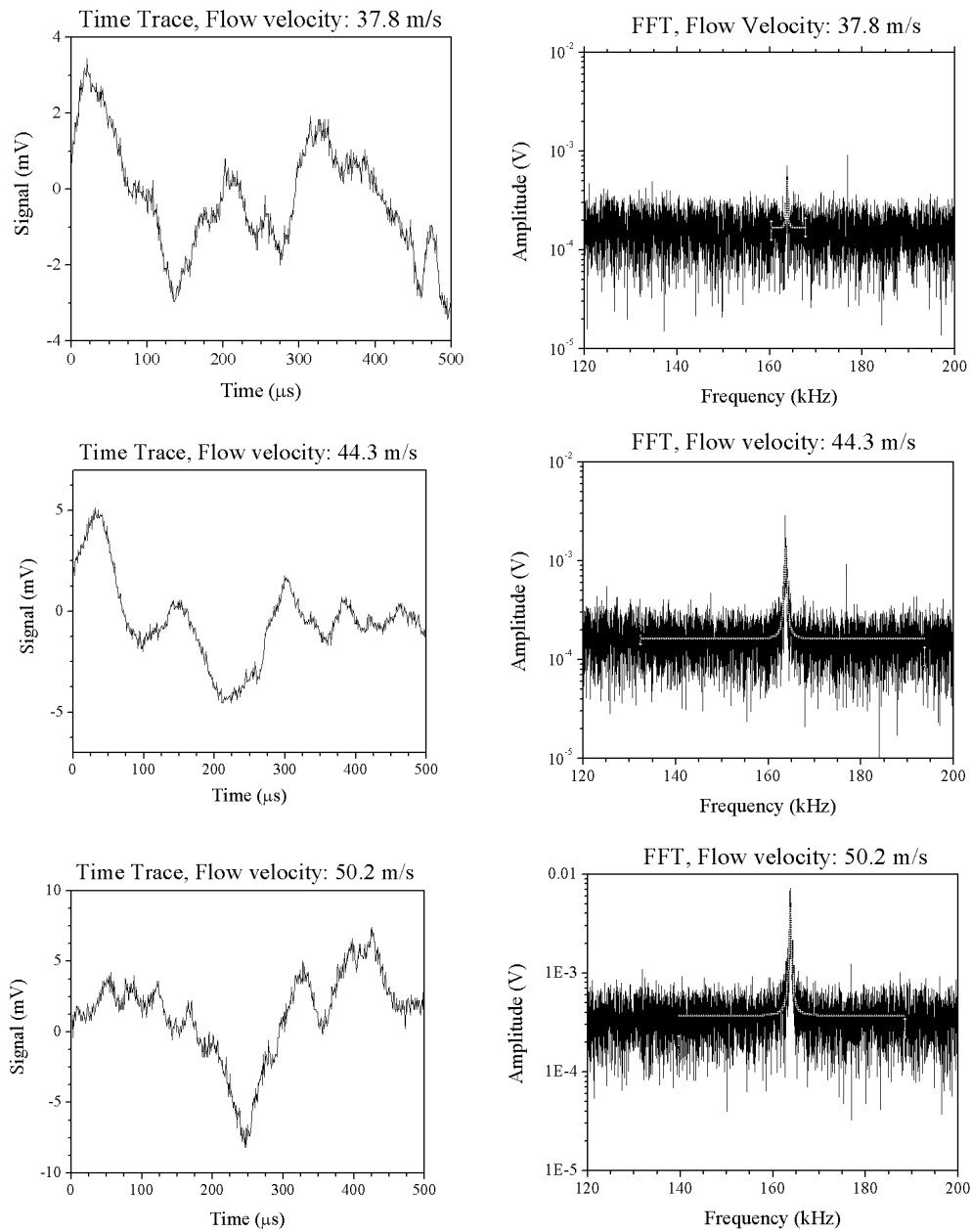


Figure 4-3: Time and frequency domain data for cantilever 6

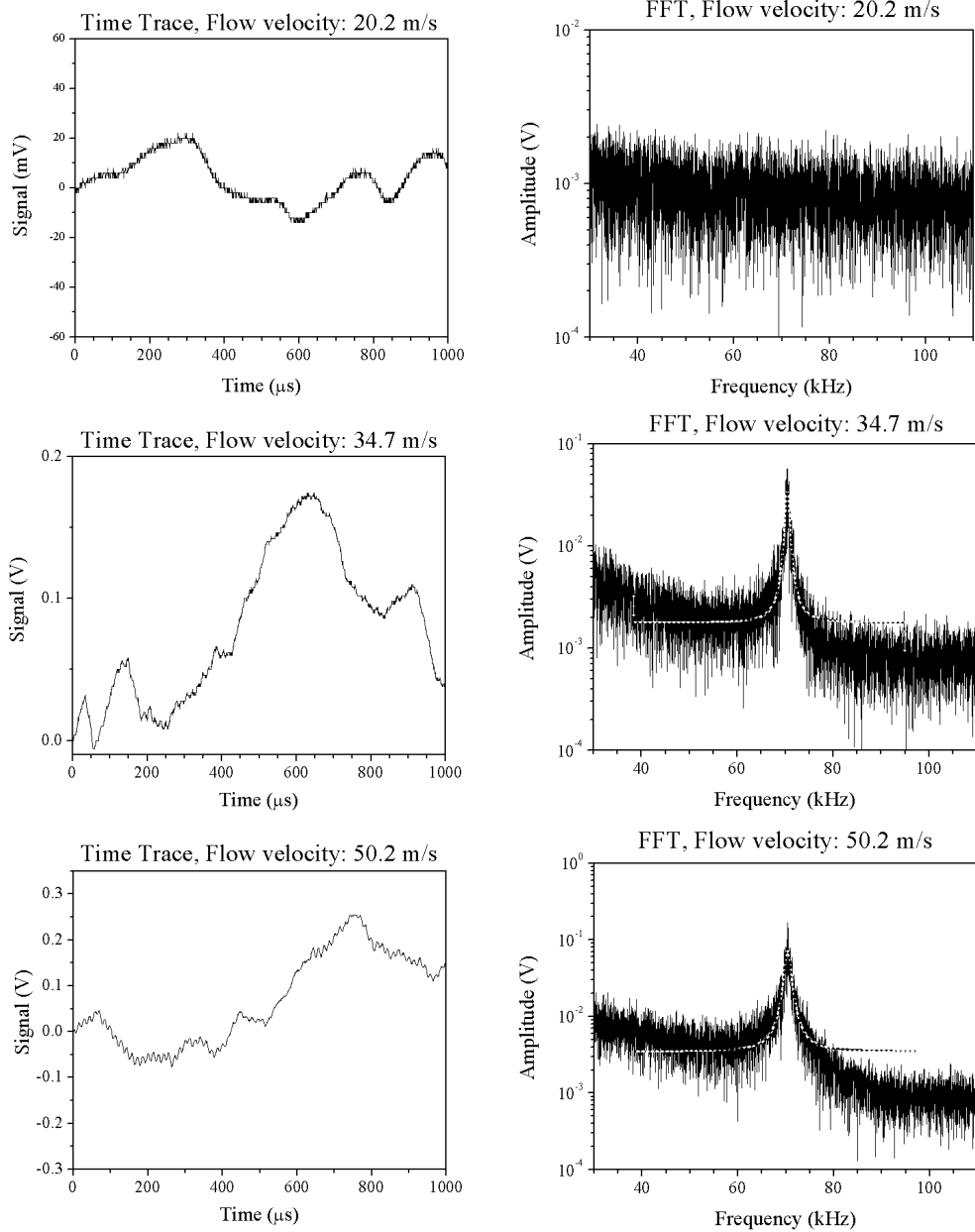


Figure 4.4: Time and frequency domain data for cantilever 7

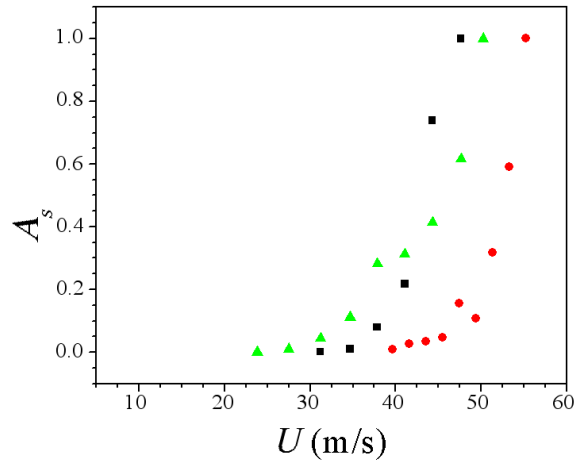


Figure 4-5: Scaled amplitude as a function of flow velocity.

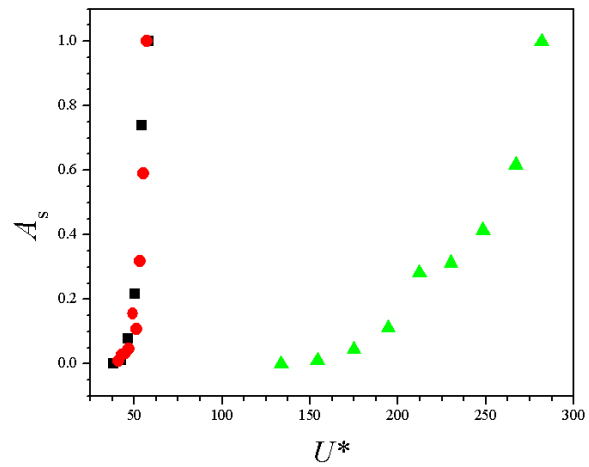


Figure 4-6: Scaled amplitude as a function of dimensionless flow velocity.

the flow system, which is 200 kPa. The density is therefore

$$\rho = \frac{P_{in}}{rT} = \frac{200,000 \text{ Pa}}{287\text{m}^2/\text{K}\cdot\text{s}^2 \times 293 \text{ K}} = 2.38\text{kg}/\text{m}^3 \quad (4.2)$$

The frequency of periodic motion for each cantilever was found to be fairly consistent regardless of flow velocity, as shown in figure 4-7. In this figure, the frequency has been normalized by the resonance frequency of the cantilever. Each value is very close to 1.0, indicating resonant behavior. The frequencies vary somewhat randomly.

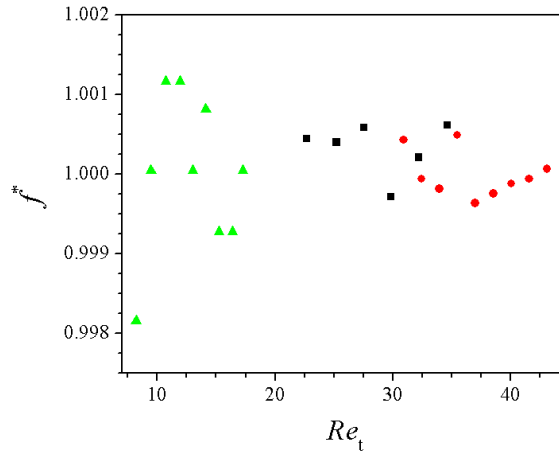


Figure 4-7: Frequency and Reynolds number data for cantilevers 1, 6, and 7.

However, cantilevers 1 and 6 both have small sections of linear increase in frequency past a certain Reynolds number.

In order to most accurately represent the Reynolds number, the mounting angle, shown in table 3.2 above, must be taken into account. Instead of the thickness of the cantilever, the projection D_b of the cantilever across the stream is used as a characteristic length in figure 4-8. D_b is defined as

$$D_b = w \sin \theta + t \cos \theta \quad (4.3)$$

where θ is the mounting angle shown in table 3.2. These projected widths are shown

in table 4.1.

Cantilever	Projection Width (μm)
1	13.1
6	6.2
7	2.9

Table 4.1: Projection Widths

This increases the Reynolds number for cantilever 1 significantly, as its mounting angle is much larger than the others.

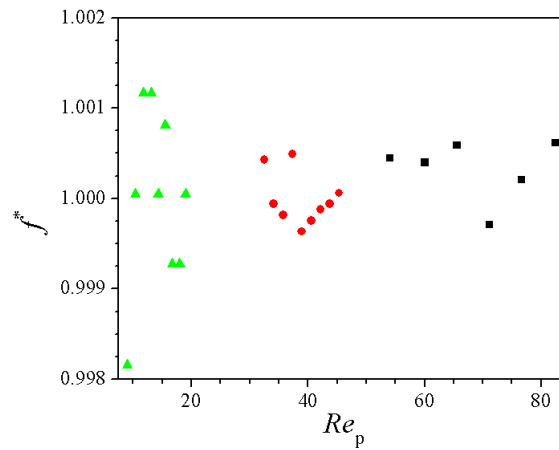


Figure 4-8: Frequency and Reynolds number in reference to stream projection width.

Figure 4-9 shows the dimensionless amplitude for each Reynolds number. While figure 4-9 has a better representation of the Reynolds numbers for each cantilever, there does not appear to be any consistency as to when the onset of vibration occurs.

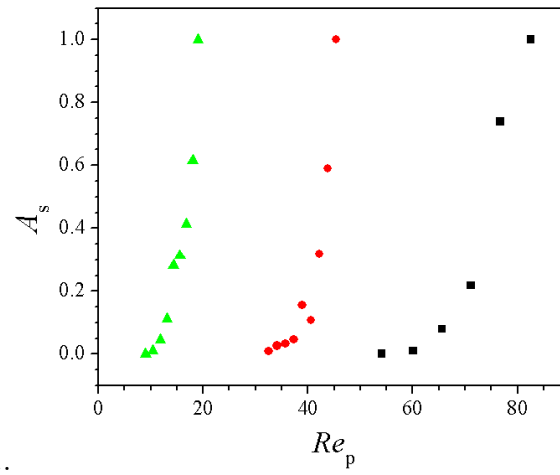


Figure 4-9: Amplitude and Reynolds number data in reference to stream projection width.

Chapter 5

Discussion of Results

5.1 Onset of Vibration

All the cantilevers tested showed vibration occurring far below the Reynolds number at which vortex shedding is expected to occur ($Re = 50$). Even accounting for the projection width as in figures 4·9 and 4·8, the Reynolds numbers at which measurable vibrations are observed for cantilevers 6 and 7 are lower than any value found in the literature for vortex shedding. As a result, predicting the vortex shedding frequency for these flows, as is done in other studies, becomes difficult, as a low Reynolds number for Strouhal number studies of rectangular cylinders begins as high as 70 (Feng, 1969; Fujarra et al., 2001; Okajima, 1982).

5.2 Lift and Dynamic Pressures

The time traces of the deflections of the cantilevers are, for the most part, dominated by noise. This indicates a marked difference from previous macroscopic studies of vortex-induced vibrations, which display limited noise response. The only exception to this is cantilever 1, which, at high flow velocities, has a significantly larger periodic response than noise response when compared to the other cantilevers. This is likely due to its mounting angle of 9.6 degrees. At this angle of attack, the aerodynamic lift of the cantilever is nonzero, and the lift force acting on the cantilever is likely to cause oscillation at its resonance frequency. Applying the thin airfoil formula for an

angle of attack a , we can find the lift coefficient

$$C_L = 2\pi a \quad (5.1)$$

The relative amplitude A_r is defined as

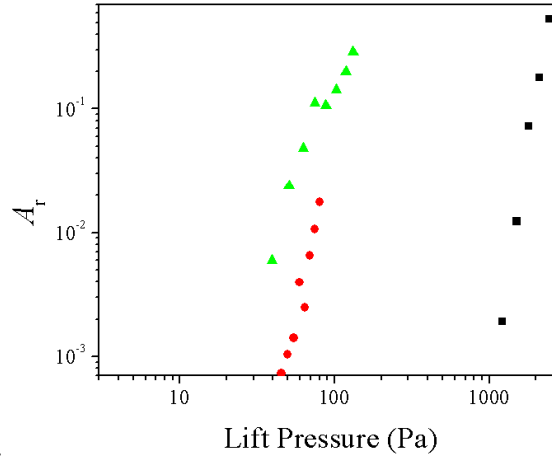


Figure 5.1: Relative amplitude as a function of lift pressure for cantilevers 1, 6, and 7.

$$A_r = \frac{A}{A_{RMS}} \quad (5.2)$$

A_r as a function of the lift pressure

$$P_L = \frac{1}{2}\rho U^2 C_L \quad (5.3)$$

is shown in figure 5.1. While there is little correlation between the cantilevers, the graph does demonstrate that the relative amplitude depends strongly on lift pressure. However, because the lift pressure is simply the lift coefficient defined in equation 5.1 multiplied by the dynamic pressure,

$$P_d = \frac{1}{2}\rho U^2 \quad (5.4)$$

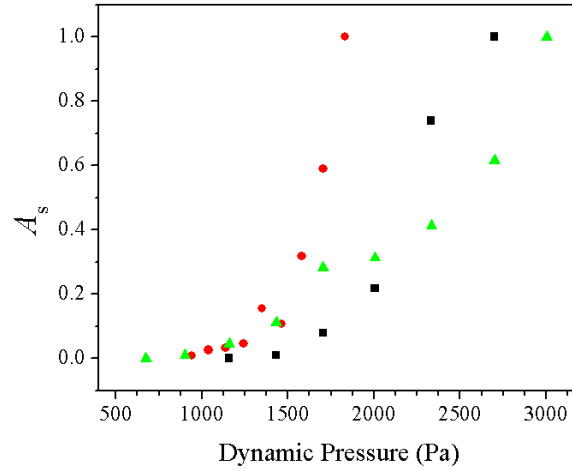


Figure 5.3: Dimensionless amplitude and dynamic pressure.

with a very clear peak at the natural frequency. While a peak has been observed, the dirty nature of each one makes it less like a self-sustaining oscillator. Moreover, the time-domain signal from each of the cantilevers shows vibrations whose center varies widely they are not symmetric about the zero point, as seen in figures 4.3 and 4.4. This is true to a lesser extent in figures 4.1 and 4.2. Additionally, the amplitudes of each cantilever's resonant vibration has shown no sign of a limit. None of the cantilevers reached a point at which the amplitude of the vibration leveled off or began to decrease as Reynolds number increased. The vibrations have been consistent with the Van der Pol oscillator in that they vibrate at frequencies close to the natural frequency, but this is the least unique aspect of the Van der Pol oscillator and is found in any system that displays resonance.

5.4 Turbulence Force

Given the high noise level and low Reynolds number in reference to the cantilever's projection width, it is unlikely that these vibrations can be ascribed to vortex shedding. Another possible explanation is that turbulence in the macroscopic flow through the flow chamber causes the local velocity to vary in direction, as shown in figure 5.4.

The component striking the face of the cantilever, transverse to the main flow direction, would apply a turbulence force F_t . This force will be proportional to the square

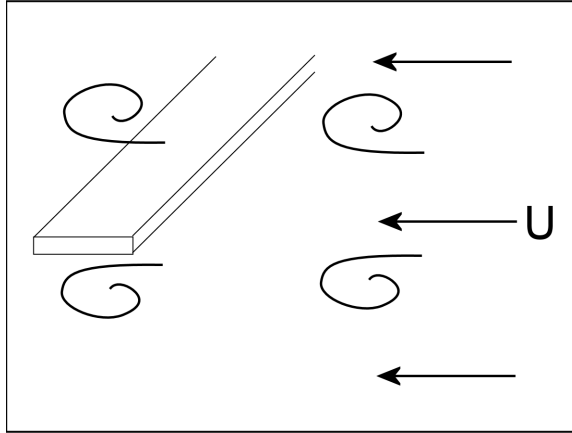


Figure 5-4: Turbulence in the macroscopic flow induces a varying force on the face of the cantilever.

of the local velocity and will cause the cantilever to deflect. Because of the high Q factor of the cantilever, the deflection induces a vibration that does not die down quickly. The time scale of the decay of the oscillations can be estimated based on the cantilever's Q factor for vibrations induced by thermal noise. This data was taken for cantilever 1 and is shown in figure 5-5. The decay of a 1-dimensional damped

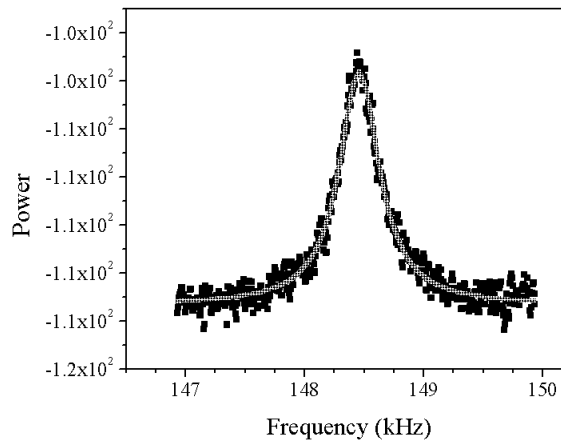


Figure 5-5: Thermal noise oscillations for cantilever 1. The quality factor of the Lorentz fit function is 365.

harmonic oscillator like the one described by equation 2.4 is given by

$$e^{-\zeta\omega_n t} \quad (5.5)$$

where ζ is defined as

$$\zeta = \frac{1}{2Q} \quad (5.6)$$

The time in seconds for cantilever 1 to decay by a factor of $1/e$ is then

$$\frac{2Q}{\omega_n} = 7.8 \times 10^{-4} \quad (5.7)$$

The time traces shown in figure 4.1 show that the noise has components that change significantly in less than the 700 microsecond time scale from equation 5.7. If this noise represents the turbulence force described above, the fundamental mode of the cantilever does not have time to decay significantly before a change in F_t induces further vibrations.

The force due to turbulence F_t is not easy to predict with the information available; the local velocity near the cantilever is unknown. If it is assumed that the local velocity against the face of the cantilever will be proportional to U , then the dynamic pressure induced by it will be proportional to the dynamic pressure of the flow. Figure 5.3 would therefore be a suitable representation of the vibration amplitude as a function of F_t .

When discussing turbulence in the flow prior to its incidence on the cantilever's leading edge, it is important to have an idea of what that turbulence is. The amplitude of the vibration as a function of the Reynolds number of the flow in reference to the channel's characteristic length of 500 microns is shown in figure 5.6. It is important to note that, for all of these cantilevers, the oscillations begin occurring at $Re > 2000$, where the flow is firmly in the turbulent regime.

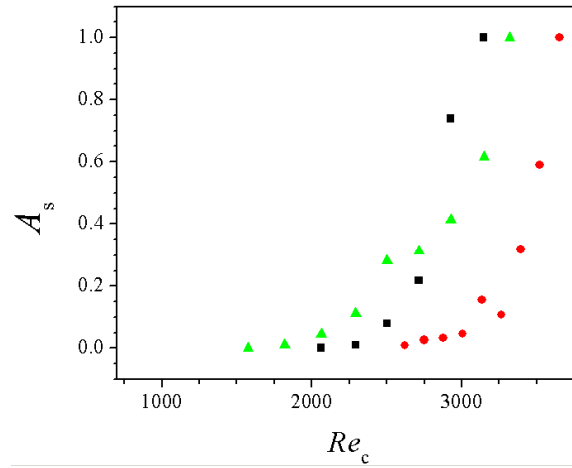


Figure 5·6: Scaled amplitude as a function of the Reynolds number in reference to channel dimensions.

Chapter 6

Conclusion

Based on these results, it is most likely that the vibrations observed in the flow are primarily due to turbulence. While vortex-induced vibration remains a possibility, the fact that the vibrations begin at Reynolds numbers below 50 for some cantilevers makes it unlikely. In addition, the slight linear increase of vibration frequency with Reynolds number in figure 4-8 is not consistent with the characteristics of classical vortex induced vibration, for the entrainment of the vortex shedding frequency to the natural frequency is not seen. However, these do not cover the entire range of data points, and due to the small number of samples and very small range of frequencies comprising this linear relationship, it may be coincidental. It should therefore not be taken as ironclad evidence against vortex induced vibration.

In order to confirm or disprove the hypothesis of turbulence-induced vibration, several further studies could be conducted. A computational fluid mechanics simulation in three dimensions would be capable of answering the question of what magnitude of force is being applied to the cantilever as a function of flow rate. This pressure function could be calculated over the entire surface of the cantilever as a function of time or in the frequency domain.

The time-domain pressure over the surface of a fixed plate of identical geometry to a cantilever could be used as the input function for convolution with the appropriate impulse response. If this results in deflections similar to the ones recorded here, that would further suggest that the hypothesis is correct.

A possible experiment to conduct would be to better determine the nature of the

flow field around the cantilever. A flow visualization method such as particle image velocimetry could determine whether the vibrations of the cantilever correspond in real time with passing eddies in the transverse direction. However, an extremely rapid frame rate, faster than the natural frequency of the cantilever, would be necessary to gain useful information from this method.

A more economical experiment would be to use a hot wire anemometer to measure the flow velocity near the cantilever. This would be a far simpler way to achieve the necessary speed of measurement. However, the hot wire anemometer is unable to measure multidimensional flow fields.

If a definitive answer is found, these results could have applications in flow field measurement. If the behavior of the cantilever can be predicted for a broader range of flow velocities than the laminar regime, the vibration of the microcantilever could be used as a tool to measure the flow velocity indirectly.

References

- Bearman, P. W. (1984). Vortex shedding from oscillations of bluff bodies. *Annual Review of Fluid Mechanics*, 16:195–222.
- Feng, C. C. (1969). The measurement of vortex induced effects in flow past stationary and oscillating circular and d-section cylinders. Master’s thesis, University of British Columbia.
- Fujarra, A. L. C., Pesce, C. P., Fleming, F., and Williamson, C. H. K. (2001). Vortex induced vibration of a flexible cantilever. *Journal of Fluids and Structures*, 15:651–658.
- Garcia-Valenzuela, A. (1997). Limits of different detection schemes used in the optical beam deflection method. *Journal of Applied Physics*, 82:985.
- Ginsberg, J. H. (2001). *Mechanical and Structural Vibrations*. John Wiley and Sons.
- Hopcroft, M. A., Nix, W. D., and Kenny, T. W. (2010). What is the young’s modulus of silicon? *Journal of Microelectromechanical Systems*, 19(2).
- Jana, A., Raman, A., Dhayal, B., Tripp, S. L., and Reifenberger, R. G. (2007). Microcantilever mechanics in flowing viscous fluids. *Applied Physics Letters*, 90.
- Okajima, A. (1982). Strouhal numbers of rectangular bodies. *Journal of Fluid Mechanics*, 123:379–398.
- Paolino, P., Tiribilli, B., and Bellon, L. (2009). Direct measurement of spatial modes of a microcantilever from thermal noise. *Journal of Applied Physics*, 106.
- Sohankar, A., Norberg, C., and Davidson, L. (1997). Numerical simulation of unsteady low-reynolds number flow around rectangular cylinders at incidence. *Journal of Wind Engineering and Industrial Aerodynamics*, 69-71:189–201.
- Williamson, C. H. K. (1988). Defining a universal and continuous strouhal-reynolds number relationship for the laminar vortex shedding of a circular cylinder. *Physics of Fluids*, 31(10).
- Williamson, C. H. K. and Govardhan, R. (2004). Vortex induced vibrations. *Annual Review of Fluid Mechanics*, 36:413–455.

